

Resolving exciton and polariton multi-particle correlations in an optical microcavity in the strong coupling regime

Victoria Quirós-Cordero,^{1,*} Esteban Rojas-Gatjens,^{2,3,*} Martin Gomez-Dominguez,¹

Hao Li,⁴ Carlo A. R. Perini,¹ Natalie Stingelin,^{1,5} Juan-Pablo Correa-Baena,¹

Eric R. Bittner,⁶ Ajay Ram Srimath Kandada,^{7,†} and Carlos Silva-Acuña^{2,4,‡}

¹*School of Materials Science and Engineering, Georgia Institute of Technology, Atlanta, GA 30332, United States*

²*School of Chemistry and Biochemistry, Georgia Institute of Technology, Atlanta, GA 30332, United States*

³*School of Physics, Georgia Institute of Technology, Atlanta, GA 30332, United States*

⁴*Institut Courtois & Département de Physique, Université de Montréal, Montréal H2V 0B3, Québec, Canada*

⁵*School of Chemical and Biochemical Engineering,*

Georgia Institute of Technology, Atlanta, GA 30332, United States

⁶*Department of Physics, University of Houston, Houston, TX 77204, United States*

⁷*Department of Physics & Center for Functional Materials,*

Wake Forest University, Winston-Salem, NC 27109, United States

(Dated: April 8, 2025)

Multi-particle correlations of exciton-polaritons and reservoir-excitons in the strong light-matter coupling regime dictate the quantum dynamics of optical microcavities. In this letter, we examine the many-body exciton-polariton dynamics in a Fabry-Pérot microcavity of a two-dimensional metal-halide semiconductor over timescales involving polariton ($\ll 1$ ps) and exciton ($\gg 1$ ps) scattering. We find enhanced exciton nonlinear dynamics in the microcavity versus the bare semiconductor, concomitant with ultrafast polariton scattering dynamics. We measure, by means of coherent spectroscopy, the coupling between exciton-polaritons, bright excitons, and reservoir-excitons that highlight the complex scattering landscape that fundamentally drives polariton condensation.

Exciton-polaritons are hybrid light-matter quasiparticles arising from the strong coupling between excitons and cavity photons, notable for their ability to undergo Bose-Einstein-like condensation at elevated temperatures [1, 2, 11]. Such condensates provide a unique platform for exploring non-equilibrium many-body physics, offering insight into quantum phase transitions, collective excitations, and spontaneous coherence in driven-dissipative systems that lie beyond the scope of traditional equilibrium condensates. The collective dynamics of exciton-polaritons are predominantly governed by microscopic energy redistribution mechanisms that funnel the population into the lowest in-plane momentum state ($k_{\parallel} = \vec{0}$), often through a complex interplay of momentum-conserving scattering pathways. These may include polariton-polariton parametric scattering and interactions with a reservoir of optically dark excitons. At their core, these processes are driven by many-body interactions mediated by multi-exciton correlations [4, 5] and the strength of the cavity-enhanced inter-excitonic Coulomb potential [6–8]. Such interactions are typically modeled within perturbative mean-field frameworks, most notably via the Gross-Pitaevskii equation. However, fundamental questions remain regarding the validity of these approaches, as direct experimental access to the underlying interaction energetics and correlation timescales remains limited.

Exciton-polariton dynamics are typically measured by time-resolving emission and transient absorption signatures of the photogenerated population with a near-impulsive photoexcitation. Although they provide valu-

able insights into the nonlinear population dynamics, accessing the underlying correlations is challenging. Moreover, these dynamics evolve on the timescales of the exciton lifetimes and are often indicative of the population in the exciton reservoir, which manifests through the spectroscopic signatures of polaritons. In this context, coherent nonlinear spectroscopy offers superior sensitivity to multi-particle correlations, as it directly probes phase-coherent nonlinear response functions that encode the temporal evolution of excited-state coherences and interaction-induced couplings beyond population dynamics. The time resolution of the experiment also enables one to explore the dynamics within the polariton lifetime, thus reducing the contributions from the reservoir.

To date, most advanced spectroscopic investigations of exciton-polaritons have focused on either GaAs quantum-well microcavities or molecular (organic) polaritons. In GaAs systems, the relatively low exciton binding energy results in weaker light-matter coupling, making it difficult to access many-body polariton dynamics using optical probes. Organic polaritons, while benefiting from stronger coupling, are hindered by broad inhomogeneous linewidths and intrinsically weak inter-excitonic interactions, which limit the resolution of coherent many-body effects [3–5, 12–14]. In this work, we instead employ two-dimensional metal halide (2DMH) perovskites as an alternative yet effective platform for exploring polariton many-body dynamics. Prototypical 2DMHs such as (PEA)₂PbI₄ (PEA = phenylethylammonium) combine several key attributes favorable for polariton condensation, including large exciton binding en-

ergies (> 200 meV), high oscillator strengths, and minimal Stokes shifts. Crucially, these materials also exhibit pronounced multi-exciton correlations [1, 2, 16, 18], positioning them as ideal candidates for studying interaction-driven exciton-polariton dynamics beyond the mean-field regime.

We investigate the many-body dynamics of photoexcitations on femtosecond to picosecond timescales in a Fabry-Pérot microcavity of $(\text{PEA})_2\text{PbI}_4$, using two-dimensional coherent electronic spectroscopy and excitation correlation photoluminescence (ECPL), respectively. At long timescales ($\gg 1$ ps), exciton-exciton interactions in the reservoir are enhanced by the cavity. On sub-picosecond timescales, we observe rapid population transfer into the lower polariton branch, followed by depopulation of the $\vec{k}_{\parallel} = \vec{0}$ state via strong polariton-polariton scattering, likely driven by repulsive Coulomb interactions. Two-quantum spectral features confirm Coulomb-mediated self- and cross-correlations between polaritons and the exciton reservoir. These results directly reveal multi-particle scattering pathways that govern the occupancy of the lowest-energy polariton states in 2D metal-halide microcavities.

A schematic of the $(\text{PEA})_2\text{PbI}_4$ microcavity studied in this work is included in Fig. 1(b). The reflectance energy dispersion shows four bands corresponding to an upper, two middle, and a lower polariton branch (Fig. 1(c), right panel). The multiple polaritons arise from the coupling of the microcavity optical mode (opt) with three excitonic features of $(\text{PEA})_2\text{PbI}_4$ [19–23], clear in the low-temperature absorption spectrum (X_A , X_B , and X_C in Fig. 1(c), left panel). The energy dispersion of the microcavity agrees with the eigenstates of a Hamiltonian in which the three excitons couple independently to a unique optical mode (white solid lines in Fig. 1(c)) [24]. The theoretical microcavity quality factor is $Q \approx 68$, which corresponds to an optical mode lifetime $\tau_{\text{opt}} \approx 37$ fs and a lower polariton lifetime $\tau_{\text{LP}} \approx 114$ fs (see the Supplementary Material [24]). This implies that measurements on picosecond timescales resolve the exciton reservoir dynamics imprinted in the lower polariton.

Under non-resonant excitation conditions, we observe that the photoluminescence (PL) arises predominantly from the lowest-energy states ($|\vec{k}_{\parallel}| < 10 \mu\text{m}^{-1}$) of the lower polariton branch, Fig. 2(a-c). The maximum PL intensity ($I_{\text{PL,max}}$) at distinct in-plane wavevectors follows different trends as a function of excitation fluence, with high wavevectors showing a clear sublinearity (Fig. 2(d)). Importantly, the PL of bare $(\text{PEA})_2\text{PbI}_4$ thin films exhibits a secondary emission at 2.31 eV (left panel, Fig. 1(c)) that grows with increasing fluence (Fig. S3 [24]) and contributes to the radiative pumping of exciton-polaritons at small \vec{k}_{\parallel} . Note that exciton-polariton condensation was not attained in this system.

We identify the exciton reservoir nonlinear dynam-

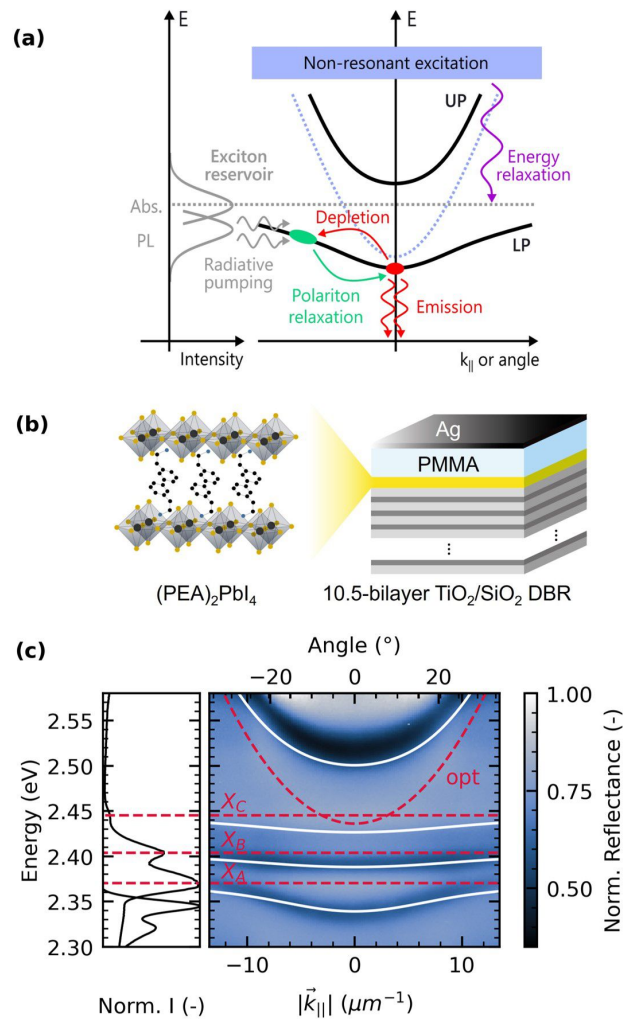


FIG. 1. (a) Competing mechanisms populating and depopulating the lower polariton $\vec{k}_{\parallel} = \vec{0}$ state for a strongly-coupled single excitonic transition (LP: lower polariton, UP: upper polariton). (b) Fabry-Pérot $(\text{PEA})_2\text{PbI}_4$ microcavity consisting of a bottom quarter-wave distributed Bragg reflector (comprising 10.5 bilayers of $\text{TiO}_2/\text{SiO}_2$ represented in dark and light gray, respectively, with a central wavelength of 520 nm), a 60 nm $(\text{PEA})_2\text{PbI}_4$ film, a 125 nm poly(methylmethacrylate) spacer layer, and a 40 nm Ag film. (c) The reflectance energy dispersion at 5 K (right panel) shows an upper, two middle, and a lower polariton branch, distinct from the microcavity optical mode (opt) and the exciton resonances (X_A , X_B , and X_C). The eigenstates of a Hamiltonian where three excitons couple to a single optical mode (solid white lines) are overlaid. The left panel includes the absorption (top) and photoluminescence (bottom) spectra of the 60 nm $(\text{PEA})_2\text{PbI}_4$ film.

ics, imprinted in the emission of the lower polariton ($\gg 1$ ps), and compare them to those of excitons in a bare $(\text{PEA})_2\text{PbI}_4$ film. For this purpose, we use excitation correlation PL (ECPL) spectroscopy, which estimates the fraction of nonlinear PL resulting from two tempo-

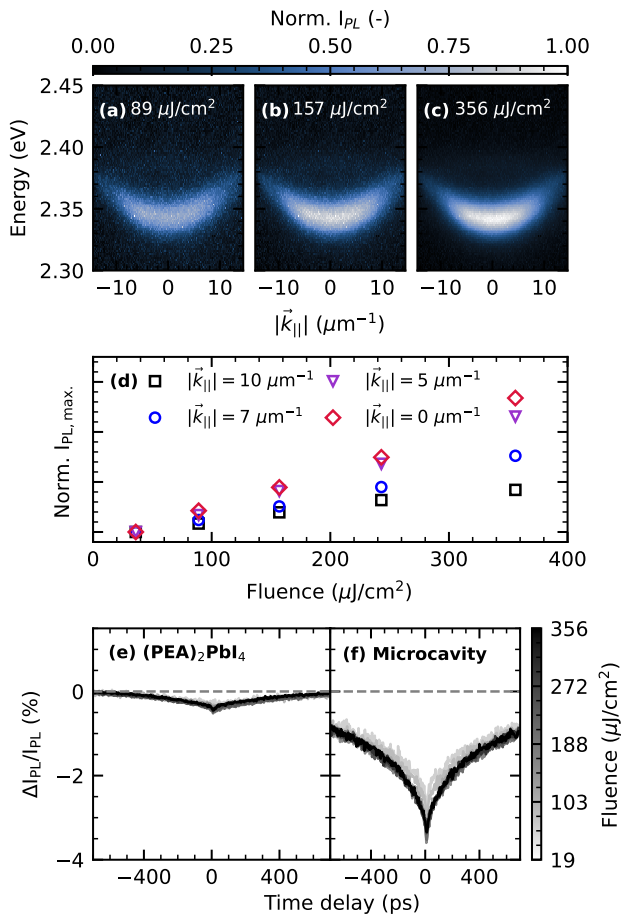


FIG. 2. (a-c) Normalized photoluminescence energy dispersion at distinct incident excitation fluences. (d) Fluence dependence of the maximum PL intensity ($I_{\text{PL,max}}$) for in-plane wavevectors 0, 5, 7, and $10 \mu\text{m}^{-1}$. To ease the comparison between the trends, we normalized $I_{\text{PL,max}}$ by its value at the lowest fluence measured. (e-f) Fraction of nonlinear PL ($\Delta I_{\text{PL}}/I_{\text{PL}}$), measured via ECPL, in a bare $(\text{PEA})_2\text{PbI}_4$ film and the microcavity. The PL energy dispersion and the ECPL experiments share the same non-resonant excitation (2.638 eV, 200 fs) and collection conditions; however, for the ECPL measurements, we integrate the PL of the entire lower polariton branch.

rally delayed excitation pulses [12, 25, 26]. In the bare $(\text{PEA})_2\text{PbI}_4$ film, we measure a small negative signal for all time delays and incident fluences, $|\Delta I_{\text{PL}}/I_{\text{PL}}| < 0.5\%$ in Fig. 2(e). In the microcavity, we observe a negative nonlinear contribution that is one order of magnitude greater than that measured in the film, $|\Delta I_{\text{PL}}/I_{\text{PL}}| < 4\%$ in Fig. 2(f). The magnitude of the negative nonlinear PL signal is indicative of the extent of exciton-exciton annihilation in each system [12, 24], suggesting increased interactions in the exciton reservoir compared to excitons in $(\text{PEA})_2\text{PbI}_4$. We rationalize the exciton-exciton annihilation increase in the microcavity due to the spatial delocalization of the exciton reservoir via population

exchange with polaritons. This hypothesis goes in line with recent work reporting a rapid exchange between polaritons and exciton-polariton transport at timescales beyond the polariton lifetime driven by the exciton reservoir [28–31].

We explore the polariton nonlinear dynamics by using coherent two-dimensional spectroscopy. The ~ 20 fs pulses [24] are resonant with the lower and first middle polariton (LP and MP_1) branches at small incidence angle ($\vec{k}_{\parallel} \approx \vec{0}$), as well as with the X_A exciton reservoir (Fig. 3(c)). The duration of the pulse and thus the temporal resolution of the experiment are shorter than the lower polariton lifetime, estimated to be $\tau_{\text{LP}} \approx 114$ fs in the $(\text{PEA})_2\text{PbI}_4$ microcavity.

We show, in Fig. 3, the one-quantum (1Q) rephasing spectra of the microcavity collected in transmission at $\vec{k}_{\parallel} \approx \vec{0}$. In 1Q experiments, we scan the time evolution of coherent states with a single-step excitation ($t_{1\text{Q}}$ in Fig. 3(g)); the time-domain function measured in the $t_{1\text{Q}}$ variable contains the excitation-energy spectral information in the Fourier domain. We measure the amplitude and phase of the coherent four-wave-mixing signal $S_{\text{FWM}}(\vec{k}_{\text{FWM}})$ spectrum at each $t_{1\text{Q}}$ and at fixed population waiting times t_{pop} . The result after a Fourier transform in $t_{1\text{Q}}$ are two-dimensional maps correlating the absorption and emission energies of single-excitation transitions.

At early population times ($t_{\text{pop}} = 20$ fs), we observe three main features along the diagonal with energies of 2.342, 2.371, and 2.390 eV (Figs. 3(a-b)) assigned to LP, the X_A reservoir, and MP_1 , respectively, in correspondence with the reflectance of the microcavity at $\vec{k}_{\parallel} = \vec{0}$, Fig. 3(c), and the absorption of $(\text{PEA})_2\text{PbI}_4$ (Fig 1(c)). The clear feature corresponding to X_A states can be rationalized through exciton-polariton models that include disorder (i.e., inhomogeneous broadening) in the exciton reservoir [32, 33] and has also been seen in two-dimensional coherent spectroscopy measurements of a strongly-coupled organic microcavity [34].

The real component of the 1Q rephasing spectra uncovers the phase behavior of the LP, X_A , and MP_1 signatures. At $t_{\text{pop}} = 20$ fs (Fig. 3(b)), X_A and MP_1 show dispersive lineshapes, with a π -shift difference between them. The lineshape of the LP looks more complicated, possibly due to overlapping transitions [18, 35]. As population time advances to 140 fs, Fig. 3(e), the lineshape of the LP signature declutters, and we observe a clear dispersive lineshape with the same phase as that of MP_1 . We interpret dispersive lineshapes in the real part of the 1Q rephasing spectra as signatures of excitation-induced energy shifts and dephasing [15, 37]. The π -shift difference between the polariton and X_A lineshapes indicates that LP and MP_1 experience excitation-induced blueshifts, while X_A undergoes a redshift. Dispersive lineshapes in 2D spectra caused by the blueshift of polariton states can arise due to Rabi contraction [37–39]

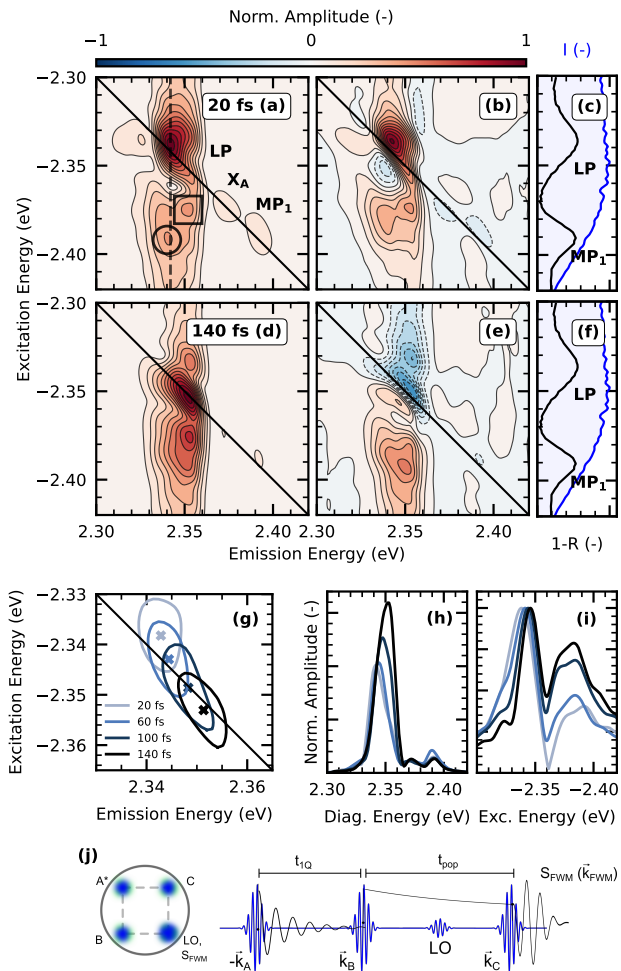


FIG. 3. 1Q rephasing spectra of the $(\text{PEA})_2\text{PbI}_4$ microcavity at 10 K, where the absolute and real components at population times (t_{pop}) of 20 fs and 140 fs are shown in (a-b) and (d-e), respectively. The dashed line corresponds to a cut along the emission energy axis at 2.342 eV. (c-f) Laser spectrum superposed with the normalized $(1-R)$ of the microcavity at $\vec{k} = \vec{0}$. The population evolution of the absolute component is summarized by tracking the (g) contour of the LP, (h) the cut along the diagonal, and (i) the vertical cut marked in (a). (j) In the experimental setup, the pulses are arranged in a *B0x-CARS* geometry (left) and time-ordered for phase-matching corresponding to the 1Q rephasing spectra (right). The pulses excite the sample at an angle of 2.3° , which corresponds to $|\vec{k}_{\parallel}| = 0.92 \mu\text{m}^{-1}$.

or polariton-polariton interactions [40]. For systems with middle polaritons (MPs), such as the one described here, Rabi contraction should lead to a blueshift of the LP and MPs and a redshift of the UP. We estimate that, in this experiment, Rabi contraction can induce a maximum energy shift of ~ 2 meV [24]. Since the estimated energy shift is smaller than the homogeneous broadening of the diagonal features, Rabi contraction will result in dispersive lineshapes instead of off-diagonal peaks. Ad-

ditionally, Fieramosca et al. [41] reported that polariton-polariton interactions in $(\text{PEA})_2\text{PbI}_4$, stemming from Coulombic effects amongst polaritons due to their excitonic constituents, induce blueshifts in the LP and MPs. The redshift of X_A can be related to exciton-exciton interactions or Coulomb mutual screening [16, 18, 42]. Separating and quantifying the mechanisms that participate in these lineshapes is not straightforward, as various processes share similar signatures and have been modeled using different levels of theory [14–16]. This endeavor is left for future work.

The population-time evolution of the absolute 1Q rephasing (Fig. S6 [24]) reveals ultrafast incoherent population transfer from X_A and MP_1 to the LP in the $(\text{PEA})_2\text{PbI}_4$ microcavity. Population transfer results in asymmetric cross-diagonal peaks, e.g. the ones marked with a square and a circle in Fig. 3(a), which indicate transfer pathways $X_A \rightarrow \text{LP}$ and $\text{MP}_1 \rightarrow \text{LP}$, respectively [44]. As population time progresses, the amplitudes of the cross-peaks increase relative to the other features in the two-dimensional map (Fig. 3(i)), supporting a downhill transfer from X_A and MP_1 to the LP occurring within a ~ 100 fs timescale. Similar scenarios have been observed in organic semiconductor microcavities [34, 35] and addressed theoretically [45]. In contrast, coherent population exchange (e.g. Rabi oscillations) between the lower and upper polariton govern the 1Q response of GaAs quantum-well microcavities [46].

Importantly, the on-diagonal LP feature displays a peculiar blueshift with increasing t_{pop} , emphasized by tracking its contour (Fig 3(g)) and the spectrum of its diagonal cut (Fig. 3(h)). The diagonal cuts at a series of population times (Fig. 3(h)), normalized at 2.340 eV (the LP energy at $\vec{k}_{\parallel} = \vec{0}$), show that the population of higher-energy larger- \vec{k}_{\parallel} LP states grows in proportion to that of $\vec{k}_{\parallel} = \vec{0}$ as t_{pop} increases. Both observations indicate a population redistribution along the lower polariton branch towards states with higher energy and $\vec{k}_{\parallel} > \vec{0}$, that is, a depletion of $\vec{k}_{\parallel} = \vec{0}$ LPs within a ~ 100 fs timescale caused by efficient polariton-polariton scattering. The growth of the population at higher in-plane wavevector states can have a contribution from the shorter lifetime of LPs at $\vec{k}_{\parallel} = \vec{0}$, due to their greater photonic component (Fig. S1) [28]. Nevertheless, we do not expect this contribution to be solely responsible for the depletion as the photonic component of the lower polariton is very similar at $\vec{k}_{\parallel} = \vec{0}$ and slightly larger \vec{k}_{\parallel} .

Using two-dimensional two-quantum (2Q) spectroscopy [47, 48], we elucidate two-particle correlations between excitons and polaritons [48–50] in the $(\text{PEA})_2\text{PbI}_4$ microcavity. For this, we utilize the pulse sequence shown in Fig. 4(f) and scan the time evolution of coherent states accessed via a two-step excitation (t_{2Q}). In the absolute 2Q spectra (Fig. 4(a)), we observe a feature on the diagonal ($E_{\text{em}} = 2E_{\text{exc}}$) corre-

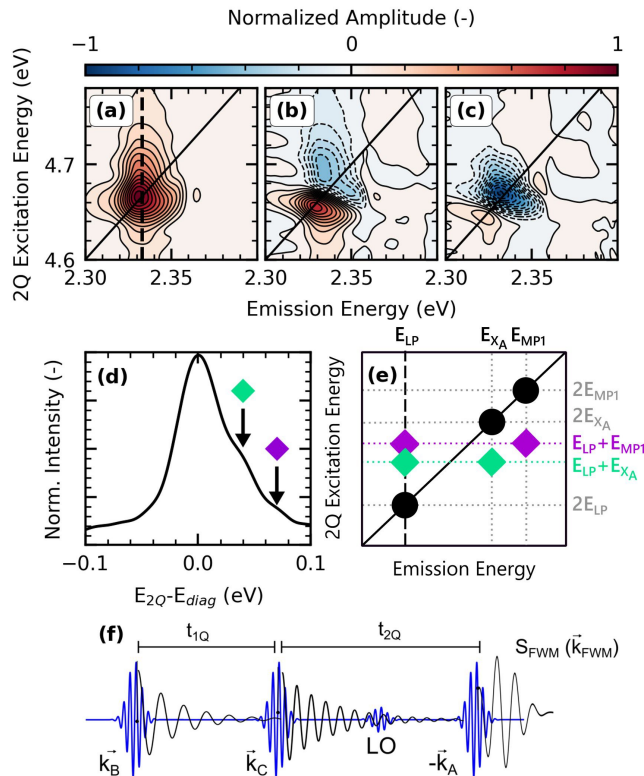


FIG. 4. (a) Absolute, (b) real, and (c) imaginary components of the 2Q non-rephasing spectra measured at $t_{1Q} = 20$ fs. (d) A cut along the emission energy axis reveals two cross-peaks with energies 32 meV (green diamond) and 65 meV (purple diamond). (e) Schematic of a two-quantum non-rephasing spectrum of a system with LP- X_A and LP- MP_1 interactions, which manifest as cross peaks with 2Q excitation energies of $E_{LP} + E_{X_A}$ and $E_{LP} + E_{MP_1}$, as indicated with green and purple diamonds respectively. (f) Schematic representation of the pulse sequence employed to measure the 2Q nonrephasing spectra, using the same phase matching of the *BoxCARS* geometry displayed in Fig. 3(h).

sponding to LP-LP self-correlations [51, 52]. We include the real and imaginary components of the two-quantum map in Figs. 4(b) and (c), correspondingly. The dispersive lineshape of the LP-LP feature in the real component of the spectrum indicates that multi-exciton interactions at the mean-field level are the principal contributors to the nonlinear signal, consistent with the prediction by Karaiskaj *et al.* [51]. We see an asymmetry stretching above the diagonal ($E_{em} = 2E_{exc}$) in the absolute (Fig 4(a)) and real component of the 2Q spectra (Fig. 4(b)). We interpret this asymmetry as two closely spaced off-diagonal peaks, clearly resolved in a vertical cut at the emission energy of 2.335 eV (dashed line in Fig. 4(a) and spectrum in Fig. 4(d)). The difference between the energies of the off-diagonal and diagonal features ($E_{2Q} - E_{diag}$) are 32 and 65 meV, which match with $E_{X_A} - E_{LP}$ and $E_{MP_1} - E_{LP}$, respectively. This suggests

that the off-diagonal features correspond to LP- X_A and LP- MP_1 two-particle states, as indicated with green and purple diamonds, correspondingly, in Figs. 4(d-e) [52]. Generally, as indicated in Fig. 4(e), at emission energies E_{X_A} and E_{MP_1} , one expects self-interactions from X_A and MP_1 (in the diagonal) and cross-correlations between LP- X_A and LP- MP_1 (asymmetries below the diagonal). We rationalize the lack of these features in the measured 2Q spectra due to the preferential excitation of the lower polariton as a consequence of the intensity distribution of our laser spectrum (Fig. 3(c)). Concisely, we demonstrate that both excitons (X_A) and middle polaritons (MP_1) act as scattering reservoirs for lower polariton states and play an integral part in the polariton dynamics of two-dimensional metal-halide microcavities.

In summary, we report the dynamics of exciton-polaritons across timescales ranging from the lower polariton lifetime at $\vec{k}_{||} = \vec{0}$ to that of the exciton. Beyond 1 ps, the behavior is largely governed by the dynamics of the reservoir population. Multiparticle interaction-driven annihilation is evident in the emission from the lower polariton state. On sub-picosecond timescales, we observe ultrafast population transfer—within 150 fs—from resonantly pumped higher-energy polariton states and reservoir populations to the $\vec{k}_{||} = 0$ state of the LP dispersion. Concurrently, LP depletion from $\vec{k}_{||} = 0$ to higher momenta ($|\vec{k}_{||}| > 0$) suggests many-body interactions driving dephasing toward the exciton reservoir [6, 7]. We also present direct evidence of many-body correlations between LP and X_A , as well as MP_1 , identifying them as Coulomb scattering baths coupled to the LP. While mean-field models capture the general polariton dynamics, they may overlook fluctuation-driven effects arising from these scattering pathways, which have a measurable impact [53–56]. Our findings on population transfer timescales and energy correlations offer a strong experimental foundation to refine these theoretical frameworks and reveal material-specific mechanisms underlying polariton condensation.

VQC, ERG, MGD, CARP, JPCB, and CSA acknowledge support from the National Science Foundation Science and Technology Center (STC) for Integration of Modern Optoelectronic Materials on Demand (IMOD) under award number DMR-2019444. VQC thanks the Georgia Tech Quantum Alliance and SPIE Optics and Photonics Education Scholarships for graduate student support. CARP acknowledges support from the National Aeronautics and Space Administration (Award#80NSSC19M0201). ERB was funded by the National Science Foundation (CHE-2404788) and the Robert A. Welch Foundation (E-1337). ARSK acknowledges start-up funds from Wake Forest University, funding from the Center for Functional Materials, and funding from the Office of Research and Sponsored Programs at

Wake Forest University. HL and CSA acknowledge funding from the Government of Canada (Canada Excellence Research Chair CERC-2022-00055). CSA acknowledges support from the Institut Courtois, Faculté des arts et des sciences, Université de Montréal (Chaire de recherche du directeur de l'Institut Courtois).

* V.Q.C. and E.R.G. are first co-authors

† srimatar@wfu.edu

‡ carlos.silva@umontreal.ca

- [1] J. Kasprzak, M. Richard, S. Kundermann, A. Baas, P. Jeambrun, J. M. J. Keeling, F. M. Marchetti, M. H. Szymańska, R. André, J. L. Staehli, V. Savona, P. B. Littlewood, B. Deveaud, and L. S. Dang, Bose–einstein condensation of exciton polaritons, *Nature* **443**, 409 (2006).
- [2] R. Balili, V. Hartwell, D. Snoke, L. Pfeiffer, and K. West, Bose–einstein condensation of microcavity polaritons in a trap, *Science* **316**, 1007 (2007).
- [11] L. Polimeno, A. Fieramosca, G. Lerario, M. Cinquino, M. De Giorgi, D. Ballarini, F. Todisco, L. Dominici, V. Ardizzone, M. Pugliese, *et al.*, Observation of two thresholds leading to polariton condensation in 2d hybrid perovskites, *Adv. Opt. Mater.* **8**, 2000176 (2020).
- [4] P. Schwendimann and A. Quattropani, Statistics of the polariton condensate, *Phys. Rev. B* **77**, 085317 (2008).
- [5] M. Pieczarka, E. Estrecho, M. Boozarjmehr, O. Bleu, M. Steger, K. West, L. N. Pfeiffer, D. W. Snoke, J. Levinsen, M. M. Parish, A. G. Truscott, and E. A. Ostrovskaya, Observation of quantum depletion in a non-equilibrium exciton–polariton condensate, *Nat. Commun* **11**, 429 (2020).
- [6] N. Takemura, M. D. Anderson, S. Biswas, M. Navadeh-Toupchi, D. Y. Oberli, M. T. Portella-Oberli, and B. Deveaud, Coherent and incoherent aspects of polariton dynamics in semiconductor microcavities, *Phys. Rev. B* **94**, 195301 (2016).
- [7] N. Takemura, M. D. Anderson, S. Trebaol, S. Biswas, D. Y. Oberli, M. T. Portella-Oberli, and B. Deveaud, Dephasing effects on coherent exciton-polaritons and the breakdown of the strong coupling regime, *Phys. Rev. B* **92**, 235305 (2015).
- [8] A. Fieramosca, R. Mastria, K. Dini, L. Dominici, L. Polimeno, M. Pugliese, C. T. Prontera, L. De Marco, V. Maiorano, F. Todisco, D. Ballarini, M. De Giorgi, G. Gigli, T. C. H. Liew, and D. Sanvitto, Origin of exciton–polariton interactions and decoupled dark states dynamics in 2d hybrid perovskite quantum wells, *Nano Lett.* **24**, 8240 (2024), pMID: 38925628.
- [3] R. T. Grant, P. Michetti, A. J. Musser, P. Gregoire, T. Virgili, E. Vella, M. Cavazzini, K. Georgiou, F. Galeotti, C. Clark, J. Clark, C. Silva, and D. G. Lidzey, Efficient radiative pumping of polaritons in a strongly coupled microcavity by a fluorescent molecular dye, *Adv. Opt. Mater.* **4**, 1615 (2016).
- [4] P. Deshmukh, L. Zhao, S. Satapathy, M. Khatoniar, B. Datta, B. P. Rand, and V. Menon, Radiative pumping of exciton-polaritons in 2d hybrid perovskites, *Opt. Mater. Express* **13**, 1655 (2023).
- [5] M. Laitz, A. E. K. Kaplan, J. Deschamps, U. Barotov, A. H. Proppe, I. García-Benito, A. Osherov, G. Grancini, D. W. deQuilettes, K. A. Nelson, M. G. Bawendi, and V. Bulović, Uncovering temperature-dependent exciton-polariton relaxation mechanisms in hybrid organic-inorganic perovskites, *Nat. Commun* **14**, 2426 (2023).
- [12] M. Maragkou, A. J. D. Grundy, T. Ostatnický, and P. G. Lagoudakis, Longitudinal optical phonon assisted polariton laser, *Appl. Phys. Lett.* **97**, 111110 (2010).
- [13] N. Somaschi, L. Mouchliadis, D. Coles, I. E. Perakis, D. G. Lidzey, P. G. Lagoudakis, and P. G. Savvidis, Ultrafast polariton population build-up mediated by molecular phonons in organic microcavities, *Appl. Phys. Lett.* **99**, 143303 (2011).
- [14] D. M. Coles, P. Michetti, C. Clark, W. C. Tsoi, A. M. Adawi, J.-S. Kim, and D. G. Lidzey, Organic semiconductors: Vibrationally assisted polariton-relaxation processes in strongly coupled organic-semiconductor microcavities, *Adv. Funct. Mater.* **21**, 3690 (2011).
- [1] F. Thouin, S. Neutzner, D. Cortecchia, V. A. Dragomir, C. Soci, T. Salim, Y. M. Lam, R. Leonelli, A. Petrozza, A. R. S. Kandada, and C. Silva, Stable biexcitons in two-dimensional metal-halide perovskites with strong dynamic lattice disorder, *Phys. Rev. Mater.* **2**, 034001 (2018).
- [2] F. Thouin, D. Cortecchia, A. Petrozza, A. R. Srimath Kandada, and C. Silva, Enhanced screening and spectral diversity in many-body elastic scattering of excitons in two-dimensional hybrid metal-halide perovskites, *Phys. Rev. Res.* **1**, 032032 (2019).
- [16] A. R. Srimath Kandada, H. Li, F. Thouin, E. R. Bittner, and C. Silva, Stochastic scattering theory for excitation-induced dephasing: Time-dependent nonlinear coherent exciton line shapes, *J. Chem. Phys.* **153**, 164706 (2020).
- [18] E. Rojas-Gatjens, H. Li, A. Vega-Flick, D. Cortecchia, A. Petrozza, E. R. Bittner, A. R. Srimath Kandada, and C. Silva-Acuña, Many-exciton quantum dynamics in a ruddlesden–popper tin iodide, *J. Phys. Chem. C* **127**, 21194 (2023).
- [19] S. Neutzner, F. Thouin, D. Cortecchia, A. Petrozza, C. Silva, and A. R. Srimath Kandada, Exciton-polaron spectral structures in two-dimensional hybrid lead-halide perovskites, *Phys. Rev. Mater.* **2**, 064605 (2018).
- [20] F. Thouin, D. A. Valverde Chávez, C. Quarti, D. Cortecchia, I. Bargigia, D. Beljonne, A. Petrozza, C. Silva, and A. Ram Srimath Kandada, Phonon coherences reveal the polaronic character of excitons in two-dimensional lead-halide perovskites, *Nat. Mater.* **18**, 349 (2019).
- [21] A. R. Srimath Kandada and C. Silva, Exciton polarons in two-dimensional hybrid metal-halide perovskites, *J. Phys. Chem. Lett.* **11**, 3173 (2020).
- [22] D. B. Straus and C. R. Kagan, Photophysics of two-dimensional semiconducting organic–inorganic metal-halide perovskites, *Annu. Rev. Phys. Chem.* **73**, 403 (2022), pMID: 35119942.
- [23] M. Dyksik, D. Beret, M. Baranowski, H. Duim, S. Moyano, K. Posmyk, A. Mlayah, S. Adjokotse, D. K. Maude, M. A. Loi, P. Puech, and P. Plochocka, Polaron vibronic progression shapes the optical response of 2d perovskites, *Adv. Sci.* **11**, 2305182 (2024).
- [24] See Supplemental Material at [URL will be inserted by publisher].
- [25] M. B. Johnson, T. C. McGill, and A. T. Hunter, Picosecond time-resolved photoluminescence using picosecond excitation correlation spectroscopy, *J. Appl. Phys.* **63**, 2077 (1988).

- [26] A. R. Srimath Kandada, S. Neutzner, V. D’Innocenzo, F. Tassone, M. Gandini, Q. A. Akkerman, M. Prato, L. Manna, A. Petrozza, and G. Lanzani, Nonlinear carrier interactions in lead halide perovskites and the role of defects, *J. Am. Chem. Soc.* **138**, 13604 (2016).
- [12] E. Rojas-Gatjens, K. M. Yallum, Y. Shi, Y. Zheng, T. Bills, C. A. R. Perini, J.-P. Correa-Baena, D. S. Ginger, N. Banerji, and C. Silva-Acuña, Resolving nonlinear recombination dynamics in semiconductors via ultrafast excitation correlation spectroscopy: Photoluminescence versus photocurrent detection, *J. Phys. Chem. C* **127**, 15969 (2023).
- [28] G. Groenhof, C. Climent, J. Feist, D. Morozov, and J. J. Toppari, Tracking polariton relaxation with multiscale molecular dynamics simulations, *J. Phys. Chem. Lett.* **10**, 5476 (2019).
- [29] R. Pandya, A. Ashoka, K. Georgiou, J. Sung, R. Jayaprakash, S. Renken, L. Gai, Z. Shen, A. Rao, and A. J. Musser, Tuning the coherent propagation of organic exciton-polaritons through dark state delocalization, *Adv. Sci.* **9**, 2105569 (2022).
- [30] D. Xu, A. Mandal, J. M. Baxter, S.-W. Cheng, I. Lee, H. Su, S. Liu, D. R. Reichman, and M. Delor, Ultrafast imaging of polariton propagation and interactions, *Nat. Commun* **14**, 3881 (2023).
- [31] L. Jin, A. D. Sample, D. Sun, Y. Gao, S. Deng, R. Li, L. Dou, T. W. Odom, and L. Huang, Enhanced two-dimensional exciton propagation via strong light-matter coupling with surface lattice plasmons, *ACS Photonics* **10**, 1983 (2023).
- [32] R. Houdré, R. P. Stanley, and M. Ilegems, Vacuum-field rabi splitting in the presence of inhomogeneous broadening: Resolution of a homogeneous linewidth in an inhomogeneously broadened system, *Phys. Rev. A* **53**, 2711 (1996).
- [33] T. Khazanov, S. Gunasekaran, A. George, R. Lomlu, S. Mukherjee, and A. J. Musser, Embrace the darkness: An experimental perspective on organic exciton-polaritons, *Chem. Phys. Rev.* **4**, 041305 (2023).
- [34] L. Mewes, M. Wang, R. A. Ingle, K. Börjesson, and M. Chergui, Energy relaxation pathways between light-matter states revealed by coherent two-dimensional spectroscopy, *Commun Phys* **3**, 157 (2020).
- [35] M. Son, Z. T. Armstrong, R. T. Allen, A. Dhavamani, M. S. Arnold, and M. T. Zanni, Energy cascades in donor-acceptor exciton-polaritons observed by ultrafast two-dimensional white-light spectroscopy, *Nat. Commun* **13**, 7305 (2022).
- [15] X. Li, T. Zhang, C. N. Borca, and S. T. Cundiff, Many-body interactions in semiconductors probed by optical two-dimensional fourier transform spectroscopy, *Phys. Rev. Lett.* **96**, 057406 (2006).
- [37] T. Yagafarov, D. Sannikov, A. Zasedatelev, K. Georgiou, A. Baranikov, O. Kyriienko, I. Shelykh, L. Gai, Z. Shen, D. Lidzey, and P. Lagoudakis, Mechanisms of blueshifts in organic polariton condensates, *Commun Phys* **3**, 18 (2020).
- [38] A. D. Dunkelberger, B. T. Spann, K. P. Fears, B. S. Simpkins, and J. C. Owrutsky, Modified relaxation dynamics and coherent energy exchange in coupled vibration-cavity polaritons, *Nature Communications* **7**, 13504 (2016).
- [39] R. T. Allen, A. Dhavamani, M. Son, S. Kéna-Cohen, M. T. Zanni, and M. S. Arnold, Population of sub-radiant states in carbon nanotube microcavities in the ultrastrong light-matter coupling regime, *The Journal of Physical Chemistry C* **126**, 8417 (2022).
- [40] Y. Sun, Y. Yoon, M. Steger, G. Liu, L. N. Pfeiffer, K. West, D. W. Snoke, and K. A. Nelson, Direct measurement of polariton-polariton interaction strength, *Nature Physics* **13**, 870 (2017).
- [41] A. Fieramosca, L. Polimeno, V. Ardizzone, L. D. Marco, M. Pugliese, V. Maiorano, M. D. Giorgi, L. Dominici, G. Gigli, D. Gerace, D. Ballarini, and D. Sanvitto, Two-dimensional hybrid perovskites sustaining strong polariton interactions at room temperature, *Sci. Adv.* **5**, eaav9967 (2019).
- [42] K. Xiao, T. Yan, C. Xiao, F. ren Fan, R. Duan, Z. Liu, K. Watanabe, T. Taniguchi, W. Yao, and X. Cui, Exciton-exciton interaction in monolayer mose₂ from mutual screening of coulomb binding (2023), arXiv:2308.14362 [cond-mat.mtrl-sci].
- [14] R. Singh, T. Suzuki, T. M. Autry, G. Moody, M. E. Siemens, and S. T. Cundiff, Polarization-dependent exciton linewidth in semiconductor quantum wells: A consequence of bosonic nature of excitons, *Phys. Rev. B* **94**, 081304 (2016).
- [44] K. Hao, L. Xu, P. Nagler, A. Singh, K. Tran, C. K. Dass, C. Schüller, T. Korn, X. Li, and G. Moody, Coherent and incoherent coupling dynamics between neutral and charged excitons in monolayer mose₂, *Nano Lett.* **16**, 5109 (2016).
- [45] D. Gallego-Valencia, L. Mewes, J. Feist, and J. L. Sanz-Vicario, Coherent multidimensional spectroscopy in polariton systems, *Phys. Rev. A* **109**, 063704 (2024).
- [46] J. Paul, H. Rose, E. Swagel, T. Meier, J. K. Wahlstrand, and A. D. Bristow, Coherent contributions to population dynamics in a semiconductor microcavity, *Phys. Rev. B* **105**, 115307 (2022).
- [47] L. Yang and S. Mukamel, Revealing exciton-exciton couplings in semiconductors using multidimensional four-wave mixing signals, *Phys. Rev. B* **77**, 075335 (2008).
- [48] P. Wen, G. Christmann, J. J. Baumberg, and K. A. Nelson, Influence of multi-exciton correlations on nonlinear polariton dynamics in semiconductor microcavities, *New J. Phys.* **15**, 025005 (2013).
- [49] K. W. Stone, D. B. Turner, K. Gundogdu, S. T. Cundiff, and K. A. Nelson, Exciton-exciton correlations revealed by two-quantum, two-dimensional fourier transform optical spectroscopy, *Acc. Chem. Res.* **42**, 1452 (2009).
- [50] T. M. Autry, G. Nardin, C. L. Smallwood, K. Silverman, D. Bajoni, A. Lemaître, S. Bouchoule, J. Bloch, and S. Cundiff, Excitation ladder of cavity polaritons, *Phys. Rev. Lett.* **125**, 067403 (2020).
- [51] D. Karaiskaj, A. D. Bristow, L. Yang, X. Dai, R. P. Mirin, S. Mukamel, and S. T. Cundiff, Two-quantum many-body coherences in two-dimensional fourier-transform spectra of exciton resonances in semiconductor quantum wells, *Phys. Rev. Lett.* **104**, 117401 (2010).
- [52] N. Takemura, S. Trebaol, M. D. Anderson, V. Kohnle, Y. Léger, D. Y. Oberli, M. T. Portella-Oberli, and B. Devaud, Two-dimensional fourier transform spectroscopy of exciton-polaritons and their interactions, *Phys. Rev. B* **92**, 125415 (2015).
- [53] M. Wouters and I. Carusotto, Excitations in a nonequilibrium bose-einstein condensate of exciton polaritons, *Phys. Rev. Lett.* **99**, 140402 (2007).
- [54] E. R. Bittner and C. Silva, Estimating the conditions for polariton condensation in organic thin-film microcavities,

- J. Chem. Phys **136**, 034510 (2012).
- [55] E. R. Bittner, S. Zaster, and C. Silva, Thermodynamics of exciton/polaritons in one and two dimensional organic single-crystal microcavities, Phys. Chem. Chem. Phys. **14**, 3226 (2012).
- [56] S. Zaster and E. R. Bittner, Role of dark excitations in the nonequilibrium condensation of exciton polaritons in optically-pumped organic single crystal microcavities, Int. J. Mod. Phys. B **29**, 1550157 (2015).

Supplemental Material: Resolving exciton and polariton multi-particle correlations in an optical microcavity in the strong coupling regime

Victoria Quirós-Cordero, Esteban Rojas-Gatjens, Martin Gomez-Dominguez, Hao Li, Carlo A. R. Perini, Natalie Stingelin, Juan-Pablo Correa-Baena, Eric R. Bittner, Ajay Ram Srimath Kandada, Carlos Silva-Acuña

MATERIALS AND METHODS

(PEA)₂PbI₄ microcavity fabrication

The microcavity comprises a bottom quarter-wavelength distributed Bragg reflector (DBR) with 10.5 pairs of TiO₂/SiO₂, a 60 nm (PEA)₂PbI₄ spin-coated film, a 125 nm poly(methyl methacrylate) (PMMA) spacer, and a top 40 nm silver mirror. The DBR has a stopband centered at 520 nm and was purchased from SpectrumThinFilms. For the microcavity preparation, first, we cleaned the DBR in sequential ultrasonic baths of acetone and IPA for 15 min each. Then, we dried it with nitrogen and treated it with UV-ozone for 15 min. The two-dimensional perovskite precursor solutions were prepared by dissolving PbI₂ (purity > 99.99%) and phenethylammonium iodide (purity > 99.99%) in N,N-Dimethylformamide (purity > 99.98%) at a 0.13 M concentration. The two-dimensional perovskite films were deposited by dropping 80 μL of precursor solution on the 1 in² clean DBRs before spin coating them at 6000 rpm for 30 s with an acceleration of 6000 rpm/s. Immediately after, the films were annealed for 10 min at 100 °C. The PMMA solution was prepared by dissolving 30 mg of PMMA (Mw ~15,000 g/mol) in 1 mL of toluene (purity > 99.98%). The PMMA solution was then deposited by spin coating. 80 μL of the solution was dropped on the two-dimensional perovskite layer and spin-coated employing a 2-step process, with an initial spreading step at 100 rpm accelerated at 1000 rpm/s for 10 s, followed by a 6000 rpm step accelerated at 6000 rpm/s. The stack was heated for 5 minutes at 60 °C to dry the PMMA film. Physical vapor deposition (PVD) was used for the top silver mirror; silver pellets (purity > 99.999%) were thermally evaporated at a rate of 0.5 angstrom/s to a final thickness of 42 nm.

Fourier imaging

Using a home-built Fourier microscope, we imaged the energy dispersion of the reflectance and photoluminescence. The microscope employs a Zeiss LD EC Epiplan Neofluar 100X infinity-corrected objective (NA = 0.75), an Acton SpectraPro 300i spectrometer, and an Andor Newton EM camera. For reflectance and photoluminescence measurements, we use a ThorLabs SLS201L broadband light source and the output of an optical parametric amplifier (ORPHEUS, Light Conversion) at 470 nm pumped by a PHAROS laser (Model PH1-20-0200-02-10, Light Conversion), respectively.

Excitation correlation photoluminescence (ECPL)

The excitation correlation photoluminescence setup used as a laser source a PHAROS (Model PH1-20-0200-02-10, Light Conversion) with an output operating at a repetition rate of 100 kHz. A portion of the laser beam was sent into a collinear optical parametric amplifier (ORPHEUS, Light Conversion) tuned for an output of 470 nm. The pulse train was then split 50/50 by a beam splitter cube, and one of the pulse trains was directed to a motorized linear stage (LTS300, Thorlabs), to impart a time delay between the two pulses. Both pulse trains were amplitude-modulated with a chopper at distinct frequencies (522 and 700 Hz). The pulse trains were then recombined and focused onto the sample using the same setup described in the Fourier Microscopy section. A flip mirror allowed us to alternate between the camera to measure the photoluminescence energy dispersion and an avalanche photodiode (APD440A, Thorlabs) for the ECPL experiment. The total integrated response was demodulated using a lock-in amplifier (HF2LI, Zurich Instruments), at the fundamental and sum of the modulation frequencies to isolate the linear and nonlinear components of the photoluminescence.

Two-dimensional coherent spectroscopy

A detailed description of the setup implemented can be found in our previous work [1, 2]. Briefly, a portion of the 1030-nm, 220-fs output of a PHAROS laser (Model PH1-20-0200-02-10, Light Conversion), operating at a 100-kHz repetition rate, was directed into a home-built third-harmonic-pumped non-collinear optical parametric amplifier. A beam geometry consisting of four pulse trains in a *BoxCARS* geometry was generated using a diffractive optical element. The four pulse trains are then sent to a home-built pulse shaper which compresses the pulses individually using a second harmonic generation chirp scan. Additionally, the pulse shaper applies a delay between the pulses and performs the phase cycle during the measurement. The resulting pulse duration was 20 fs full-width at half-maximum, measured by second-harmonic generation cross-frequency-resolved optical gating (SHG-XFROG), as characterized in Supplementary Information. All measurements were carried out in a vibration-free closed-cycle cryostat (Montana Instruments). The spot size was $95 \pm 5 \mu\text{m}$. The spectra were collected by pumping with the same laser spectrum and an incident fluence of $0.7 \mu\text{J cm}^{-2}$ per pulse. The pulses excite the sample at an angle of 2.3° , which corresponds to $|\vec{k}_{\parallel}| = 0.92 \mu\text{m}^{-1}$.

MICROCAVITY DESIGN

The energy of the microcavity optical mode was designed such that the lower polariton has good energetic overlap with the maximum emission of $(\text{PEA})_2\text{PbI}_4$ at small in-plane wavevectors. This design should facilitate the population of the lower polariton $\vec{k}_{\parallel} = \vec{0}$ state via radiative pumping [3–5] and the observation of polariton-polariton correlations.

We used the following expressions to calculate the microcavity quality factor Q , the optical mode lifetime τ_{opt} , and the lower polariton lifetime τ_{LP} :

$$Q = E_{\text{opt}}(\vec{k}_{\parallel} = \vec{0}) / \Delta_{\text{FWHM}}[E_{\text{opt}}(\vec{k}_{\parallel} = \vec{0})] \quad (\text{S01})$$

$$\tau_{\text{opt}} = 2Q / \omega_{\text{p}}(\vec{k}_{\parallel} = \vec{0}) \quad (\text{S02})$$

$$\tau_{\text{LP}} = \left[|X_{\text{opt}}|^2 / \tau_{\text{opt}} + \sum_{i=\text{A,B,C}} |X_i|^2 / \tau_{X_i} \right]^{-1} \quad (\text{S03})$$

Where $E_{\text{opt}}(\vec{k}_{\parallel} = \vec{0})$ is the optical mode energy at normal incidence according to the transfer matrix simulation detailed in the next section, $|X_{\text{opt}}|^2$ and $|X_i|^2$ are the Hopfield coefficients of the lower polariton at $\vec{k}_{\parallel} = \vec{0}$ (see the strong light-matter coupling Hamiltonian section), and τ_{X_i} is the lifetime of the excitons ($i = \text{A, B, C}$) reported in Ref. 6 at 15 K.

TRANSFER MATRIX MODEL SIMULATION

We simulated the energy dispersion of the microcavity optical mode using a transfer matrix model (TMM). We followed the TMM equations (S05) – (S09) described below and used the experimentally determined thicknesses and complex energy-dependent refractive indices of every layer in the microcavity stack, except for the $(\text{PEA})_2\text{PbI}_4$. To simulate the dispersion of the optical mode, instead of that of the polariton branches via TMM, we must consider the refractive index of $(\text{PEA})_2\text{PbI}_4$ to be static, real, and equal 2.61, which is the real refractive index of the material at the target optical mode energy of 2.436 eV. The simulated dispersion of the optical mode is shown in Fig. S3. We obtained equation (S04) describing the dispersion as a function of in-plane wavevector by fitting a polynomial to the reflectance minimum (red dashed line in Fig. S3)

$$E_{\text{opt}}(\vec{k}_{\parallel}) = \hbar\omega_{\text{p}}(\vec{k}_{\parallel}) = 2.436 + 9.679 \times 10^{-4} \vec{k}_{\parallel}^2 \text{ eV}. \quad (\text{S04})$$

Next, we summarize the main equations of the transfer matrix model. More details can be found in Ref. [7]. The optical response of a thin film can be fully described by a transfer matrix that summarizes the continuity conditions of

the electric and magnetic field components that are tangential to the film's interfaces. The angle-dependent transfer matrix of a single film is given by:

$$T_{\text{film}, s\text{-pol}} = \begin{pmatrix} \cos(\delta_{\text{film}}) & i \sin(\delta_{\text{film}})/[n_{\text{film}} \cos(\theta_{\text{film}})] \\ in_{\text{film}} \sin(\delta_{\text{film}}) \cos(\theta_{\text{film}}) & \cos(\delta_{\text{film}}) \end{pmatrix}, \quad (\text{S05})$$

$$T_{\text{film}, p\text{-pol}} = \begin{pmatrix} \cos(\delta_{\text{film}}) & i \sin(\delta_{\text{film}}) \cos(\theta_{\text{film}})/n_{\text{film}} \\ in_{\text{film}} \sin(\delta_{\text{film}})/\cos(\theta_{\text{film}}) & \cos(\delta_{\text{film}}) \end{pmatrix}, \quad (\text{S06})$$

$$\delta_{\text{film}} = \frac{2\pi n_{\text{film}} d_{\text{film}}}{\lambda} \cos(\theta_{\text{film}}), \quad (\text{S07})$$

where n_{film} corresponds to the complex energy-dependent refractive index, θ_{film} is the angle of propagation of light as given by Snell's law, and d_{film} the film thickness. This result can be extended to an assembly of q thin films, where the total transfer matrix is the product of the individual matrices, $T_{\text{assembly}} = \prod_{\text{film}}^q T_{\text{film}}$. The left-most matrix corresponds to the first film light traverses.

The reflectance (R) of a thin-film assembly can then be obtained from its transfer matrix as follows:

$$\begin{pmatrix} E_{\text{in}}/E_{\text{out}} \\ H_{\text{in}}/H_{\text{out}} \end{pmatrix} = \begin{pmatrix} B \\ C \end{pmatrix} = T_{\text{assembly}} \begin{pmatrix} 1 \\ n_s \end{pmatrix}, \quad (\text{S08})$$

$$R = \left(\frac{n_0 B - C}{n_0 B + C} \right) \left(\frac{n_0 B - C}{n_0 B + C} \right)^*, \quad (\text{S09})$$

where n_0 and n_s correspond to the refractive indices of the incident and output media (typically air and the substrate, correspondingly).

STRONG LIGHT-MATTER COUPLING HAMILTONIAN

The following multiple-exciton Hamiltonian, based on a Jaynes-Cummings model extended to three excitonic states and using the rotating wave approximation, describes the polariton branches observed in the microcavity energy dispersion. Notably, to reproduce the energy dispersion of the polariton branches observed experimentally, at least three distinct excitonic states are required.

$$\hat{H}(\vec{k}_{\parallel}) = \sum_{i=A,B,C} \hbar\omega_i b_i^\dagger b_i + \hbar\omega_p(\vec{k}_{\parallel}) a_p^\dagger a_p + \sum_{i=A,B,C} g_i (a_p^\dagger b_i + a_p b_i^\dagger). \quad (\text{S010})$$

The first term represents the creation and annihilation of excitons ($i = A, B, C$) with energy $\hbar\omega_i$ and excitonic annihilation operator b_i . The second term describes the insertion and removal of cavity-mode photons as a function of in-plane wavevector whose energy is a function of in-plane wavevector $\hbar\omega_p(\vec{k}_{\parallel})$ and with photon annihilation operator a_p . The third term describes strong exciton-photon coupling, where g_i is the coupling constant between the i -th exciton and the cavity-mode photons.

We diagonalized the Hamiltonian using the numerical package Qutip [8] and leveraged the dispersion bands to estimate coupling strengths $g_{A,B,C} = 80, 80, 90$ meV. During this process, we fixed the energy of the excitonic transitions (2.370, 2.404, and 2.445 eV) and the microcavity dispersion (calculated using the transfer matrix model as described above) while changing the coupling strengths. We emphasize that since we have three coupling strengths as variables, various combinations of them reproduce the polariton branches observed with good accuracy, and hence these coupling strengths should not be taken as definitive. However, we note that the couplings are of the order of $\approx 80 - 100$ meV and that at least three excitons are required to reproduce all polariton band energies. The simulated polariton eigenstates are shown in Fig. 1 as solid white lines overlaid to the experimental energy dispersion at 5 K. Additionally in Fig. S1, we show the Hopfield coefficients for the polariton states that diagonalize the Hamiltonian. These coefficients provide information on the photonic and excitonic components that constitute each state.

REFLECTANCE ENERGY DISPERSION

Observation of four polariton branches

We distinguish four polariton branches in the experimental energy dispersion of the microcavity: an upper (UP), two middle (MP1 and MP2), and a lower polariton. We emphasize this in Fig. S2 by displaying reflectance spectra at a series of in-plane wavevectors. Each polariton branch corresponds to a low-reflectivity peak.

Factors influencing the reflectance of polariton branches.

The difference in reflectance among polariton states is likely because of their distinct X_A , X_B , and X_C fractions ((S1)), since these excitonic constituents have different oscillator strengths. This is evidenced in the absorption spectra of $(\text{PEA})_2\text{PbI}_4$ (left panel, Fig. 2 in the main text). In addition, variations in the overlap of the polariton states with the exciton reservoirs can also lead to differences in reflectance. It has been reported previously that, in the most exacerbated case, this overlap causes “a polariton breakdown” in which the reflectance of the state vanishes [9].

PHOTOLUMINESCENCE-DETECTED TECHNIQUES

Linear measurements

We show the fluence-dependent photoluminescence (PL) spectra of the bare $(\text{PEA})_2\text{PbI}_4$ film as a function of fluence (Fig. S4), in which we observe a secondary emission assigned in the literature to a dark exciton, a biexciton state, and the overlap between both [5, 10, 11].

Additionally, we include the PL energy dispersion of the lower polariton and a spectral cut at $\vec{k}_{\parallel} = \vec{0}$ (Fig. S5, top panel) as a function of fluence. These measurements were taken under non-resonant pumping (470 nm, 220 fs), using the same laser pulse employed in the ECPL experiments, and detecting with an Andor Newton EM camera. We also display the linewidth and the maximum peak energy of the lower polariton emission as a function of fluence, extracted from Lorentzian fits to the spectra (Fig. S5, bottom panel).

Nonlinear measurements: Excitation correlation photoluminescence (ECPL) spectroscopy

Briefly, ECPL is a technique that excites the sample with two pulses, one of which is temporally delayed from the other. The pulses are amplitude-modulated at two distinct frequencies (Ω_1 and Ω_2). Then, we detect the time-integrated photoluminescence and isolate its nonlinear component by demodulating at the sum frequency ($\Omega_1 + \Omega_2$) via lock-in detection. The time resolution arises from the delay between the two pulses.

Modeling bimolecular annihilation in a semiconductor

A simple kinetic model for exciton dynamics, discussed in more detail in Ref. [12], accurately describes the ECPL traces of $(\text{PEA})_2\text{PbI}_4$ films. This model includes a monomolecular recombination term with a γ rate and an exciton-exciton annihilation term with a parameter β . The differential equation and its corresponding solution are:

$$\begin{aligned} \frac{dn}{dt} &= -\gamma n - \beta n^2 \\ n(t) &= \frac{n_0 \gamma / \beta}{(n_0 + \gamma / \beta) \exp(\gamma t) - n_0}. \end{aligned} \tag{S011}$$

From the time-dependent exciton population $n(t)$, we can obtain the total photoluminescence after the interaction with two identical laser pulses, assumed to be delta functions and, therefore, considered as initial conditions. The total photoluminescence detected is:

$$I_{\text{total PL}} \propto \int_0^{\tau} n_1(t) dt + \int_{\tau}^{\infty} n_2(t - \tau) dt. \tag{S012}$$

The first integral considers the time when only one pulse arrived at the sample and the second integral considers the time after the two incident pulses. The initial conditions correspond to $n_1(0) = n_0$ and $n_2(0) = n_1(\tau) + n_0$, where $n_1(\tau)$ is the residual population due to the sample's interaction with the first pulse. Then we subtract the single pulse contributions, $I = 2 \int_0^\infty n(t)dt = 2n_0$, to obtain the nonlinear photoluminescence:

$$\Delta I_{\text{PL}}(\tau) \propto \ln \left(1 - \frac{\alpha^2 \exp(-\gamma\tau)}{(1+\alpha)^2} \right); \quad \alpha = \frac{n_0\beta}{\gamma}. \quad (\text{S013})$$

Note that although both time-resolved photoluminescence and ECPL follow the same population, their decay functions are different and we cannot compare their decay traces directly.

Modeling the lower-polariton picosecond dynamics

We rationalize the lower-polariton picosecond dynamics by expanding the kinetic model for the semiconductor exciton dynamics. Following Ref. [13], we include a differential equation for the time evolution of the lower polariton population $p(t)$ that is coupled to the time-dependent exciton-reservoir population $n(t)$. This additional equation includes the radiative decay of the LP with a rate of γ_{LP} , bimolecular annihilation between the exciton reservoir and the lower polariton—which depends on $|X_{\text{A}}|^2$, the X_{A} fraction of the LP, and is described by the parameter β_{LP} —and a transfer rate $W_{\text{exc} \rightarrow \text{LP}}$ from the reservoir to the lower polariton.

$$\begin{aligned} \frac{dn}{dt} &= -(\gamma + W_{\text{exc} \rightarrow \text{LP}})n - \beta n^2 \\ \frac{dp}{dt} &= -\gamma_{\text{LP}}p - \beta_{\text{LP}}|X_{\text{A}}|^2 np + W_{\text{exc} \rightarrow \text{LP}}n. \end{aligned} \quad (\text{S014})$$

These coupled differential equations do not have an analytical solution. They must be solved numerically to find $p(t)$. Then, the total photoluminescence of the microcavity is given by:

$$I_{\text{total PL}} \propto \int_0^\tau p_1(t)dt + \int_\tau^\infty p_2(t-\tau)dt. \quad (\text{S015})$$

With initial conditions $p_1(0) = 0$ and $p_2(0) = p_1(\tau)$, where $p_1(\tau)$ is the residual LP population due to the sample's interaction with the first pulse. The nonlinear photoluminescence of the LP is $\Delta I_{\text{PL}} = I_{\text{total PL}} - I$, where I corresponds to the lower-polariton PL intensity originating from two single pulses and can be expressed as $I = 2 \int_0^\infty p(t)dt$. Bimolecular annihilation between lower polaritons and excitons plays a minor role since polaritons are short-lived compared to excitons. From this model, it is clear that exciton bimolecular annihilation in the reservoir is the main nonlinearity quenching the total photoluminescence of lower polaritons in picosecond timescales and leading to a negative ECPL signal.

TWO-DIMENSIONAL COHERENT SPECTROSCOPY

Characterizing pulse duration

The second-harmonic generation cross-frequency-resolved optical gating (SHG-XFROG) of the pulse employed is shown in Fig. S6, which indicates that our pulse duration is 20 fs, full-width half-maximum.

Population-time series of the microcavity's one-quantum (1Q) rephasing response

The 1Q rephasing spectra of the $(\text{PEA})_2\text{PbI}_4$ microcavity at various population times (t_{pop}) can be found in Fig. S7. Its absolute component is displayed in Fig. S7(a-d) (top row), while its real and imaginary components are included in Fig. S7(e-h) (middle row) and Fig. S7(i-l) (bottom row), respectively. We summarized the main features of the absolute 1Q rephasing spectra evolving with t_{pop} in Fig. 5 of the main text. The vertical and diagonal cuts and the lower polariton contour were extracted from the data plotted here.

Contributions to the 1Q and 2Q signals

In Fig. S8, we show the pathways contributing to the 1Q rephasing (top) and 2Q non-rephasing spectra (bottom) included in the main text. Contributions to 1Q rephasing spectra include ground-state bleach (GSB), stimulated emission (SE), and excited-state absorption (ESA), which involve both singly and doubly excited-state pathways. The 2Q spectrum solely probes doubly excited-state pathways, resolving the double excitation manifold without contributions from single excited states.

When considering the bosonic nature of excitons, ESA pathways can result in dispersive lineshapes and linewidth broadening in the 1Q rephasing spectra, as the stabilization energy of ij doubly excited states—in this work, $ij = LP, MP1, X_A, \dots$ —typically leads to a redshifted feature that overlaps with the ground-state bleach. This has been discussed by Singhet *al.* [14]. However, dispersive-like 1Q rephasing spectra are usually assigned to energy shifts that result from a convolution of different mechanisms, such as exciton-exciton interactions, background exciton scattering, and Rabi contraction. Different physical models have been presented to account for dispersive-like spectra in two-dimensional spectroscopy. This dispersive lineshape is also explained by employing phenomenological models based on modified optical Bloch equations [15] and a stochastic theory derived by some of the authors in previous works [16]. Finally, in the case of polaritons, Rabi contraction (a decrease in the Rabi splitting due to exciton photobleaching induced by the excitation) also results in dispersive lineshapes. The distinct physical processes leading to the dispersive lineshapes and the many models that describe them make the simulation theoretically demanding and outside the scope of this work. Additionally, we note that, in reality, one never has one, two, or three excitations in these systems. A proper many-body description demands that one work in the large- N limit and that excitations are taken from an ensemble of (at best) weakly interacting bosons. Recent theoretical work by Pérez [17] has explored this limit.

Rabi contraction

We estimated the Rabi contraction effect roughly, as described by equation (S018).

$$g_i = 2\Omega_i = g_0\sqrt{N_i}. \quad (\text{S016})$$

$$\Delta = 2\Omega_1 - 2\Omega_2 = g_0\sqrt{N_1} - g_0\sqrt{N_2}. \quad (\text{S017})$$

$$\Delta = g_1 \left(1 - \sqrt{\frac{N_2}{N_1}} \right), \quad (\text{S018})$$

where N_1 is the initial number of excitonic transitions and N_2 is the remaining number of transitions after excitation. We estimate N_1 using the exciton's Bohr radius (2.2 nm from 18) and assuming half-filled hexagonal packing. We note that considering higher exciton densities participating in strong coupling would lead to a smaller Rabi contraction. We multiply this number by 37, the number of metal-halide quantum wells in a 60-nm film. The number of bleached excitons N_{bl} is estimated from the experimental excitation density of $0.7 \mu\text{J cm}^{-2}$ at a center wavelength 528 nm, assuming the most drastic scenario in which all pulse energy is absorbed and only causes exciton bleaching. Then, $N_2 = N_1 - N_{\text{bl}}$. After setting the initial g_1 as 90 meV (from our simulations), the estimated effect of the Rabi contraction would be 2 meV. The shift is based on an overly estimated density and thus is an upper limit of the possible shift. Notably, even this upper estimate is too small to result in the observed cross-peaks in the rephasing spectrum presented in the manuscript. Accordingly, we can disregard Rabi contraction being the source of the observed nonlinear lineshapes.

GROSS-PITAEVSKII EQUATION WITH EXCITON DIFFUSION

$$\begin{aligned} i\hbar\partial_t\phi(x) &= \left(-\frac{\hbar^2}{2\mu}\nabla^2 + g|\phi(x)|^2 + \frac{i}{2}(rS(x) - \gamma) \right) \phi(x); \\ \partial_t S(x) &= D_s\nabla^2 S(x) - rS(x)|\phi(x)|^2 - \gamma_{SS}S^2(x) + p(x, t) - \gamma_S S(x), \end{aligned} \quad (\text{S019})$$

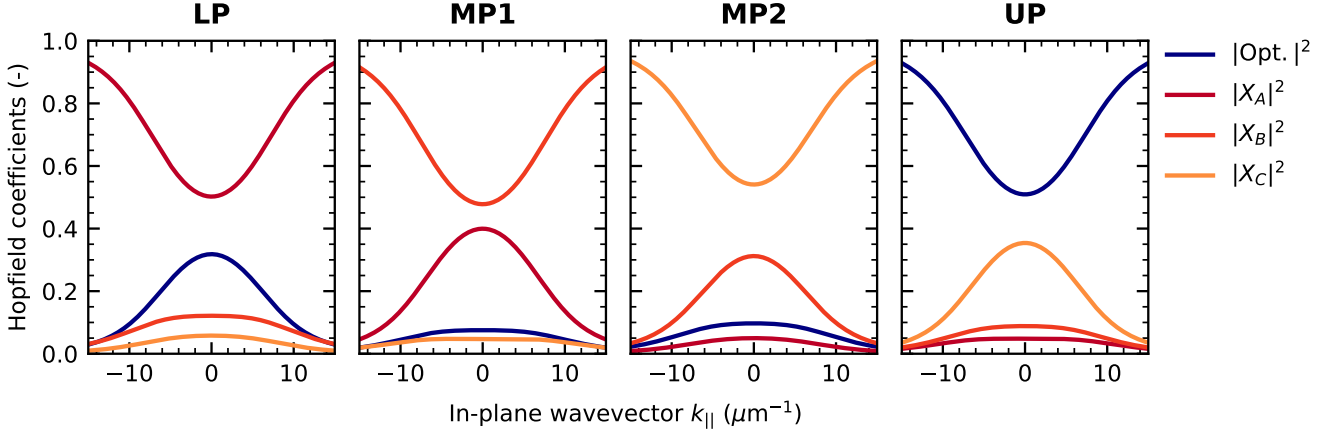


FIG. S1. **Hopfield coefficients of the polariton eigenstates.** They were calculated by numerically diagonalizing the Hamiltonian (1) of the main text using the numerical package, Qutip. The simulation details are discussed in the text above.

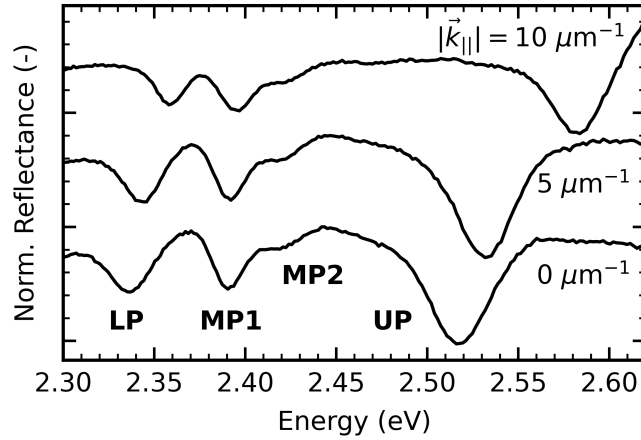


FIG. S2. **Reflectance spectra of the $(\text{PEA})_2\text{PbI}_4$ microcavity at in-plane wavevectors of 0, 5, and 10 μm^{-1} showing four polariton branches.**

where $|\phi(x)|^2$ is the condensate population and $S(x)$ is the exciton reservoir, pumped by $p(x, t)$, which has a characteristic decay rate γ_S and can interconvert with the condensate population at a bimolecular rate r . Furthermore, g is the mean-field interaction between polaritons and γ represents the losses of the condensate. The model also includes exciton-exciton annihilation depleting the exciton reservoir population with rate constant γ_{SS} . This model suggests that condensates can form when a steady-state population can be established, requiring that $(rS(x) - \gamma) > 0$ so that the rate of polariton population through the exciton reservoir outpaces the condensate's population loss.

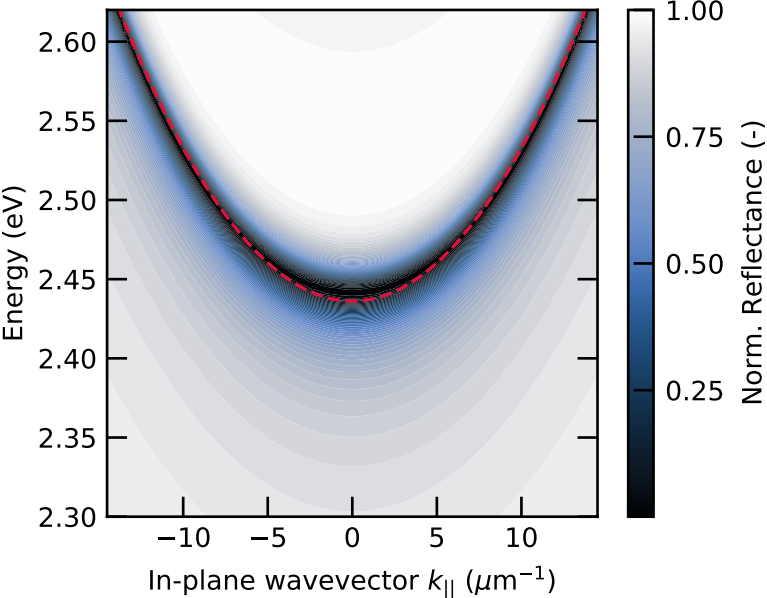


FIG. S3. **Transfer matrix model of the microcavity optical mode.** We used the TMM method described above and fitted to the simulation a quadratic polynomial (red dashed line) to get a mathematical expression for the dispersion.

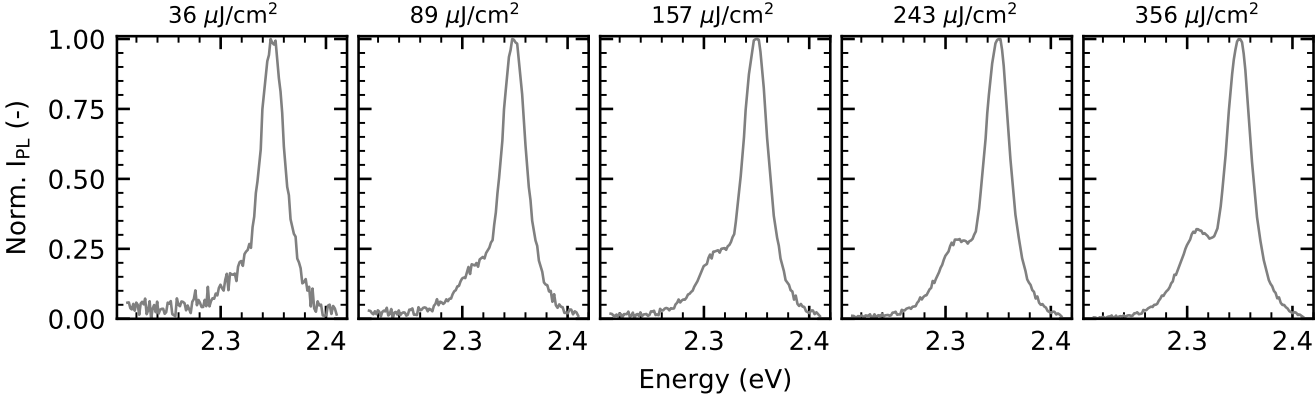


FIG. S4. **Photoluminescence spectra of a 60 nm $(\text{PEA})_2\text{PbI}_4$ as a function of fluence.** This data was taken under a non-resonant excitation (470 nm, 220 fs) with varying fluence and at a temperature of 5 K.

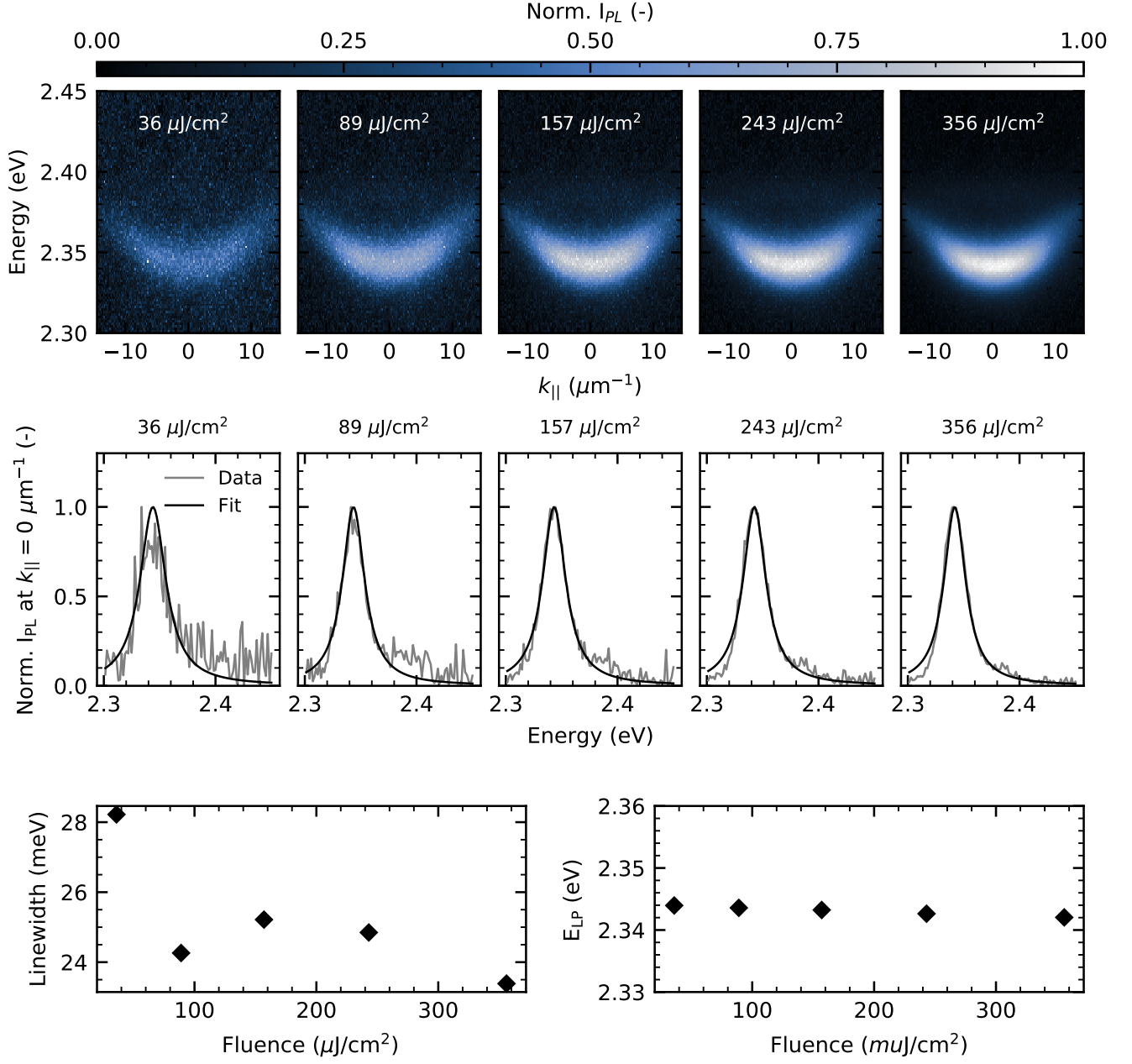


FIG. S5. **Photoluminescence energy dispersion of the lower polariton as a function of fluence.** We show the PL spectra at $\vec{k}_{\parallel} = 0$, linewidth, and energy of the $(\text{PEA})_2\text{PbI}_4$ microcavity as a function of fluence measured under non-resonant excitation (470 nm, 220 fs).

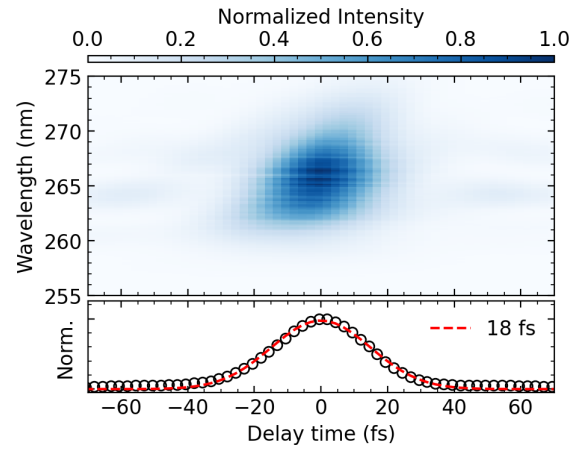


FIG. S6. **X-Frog characterization of the pulse.** The X-frog is performed by placing a thin BBO at the sample position. The durations is extracted by fitting a Gaussian function.

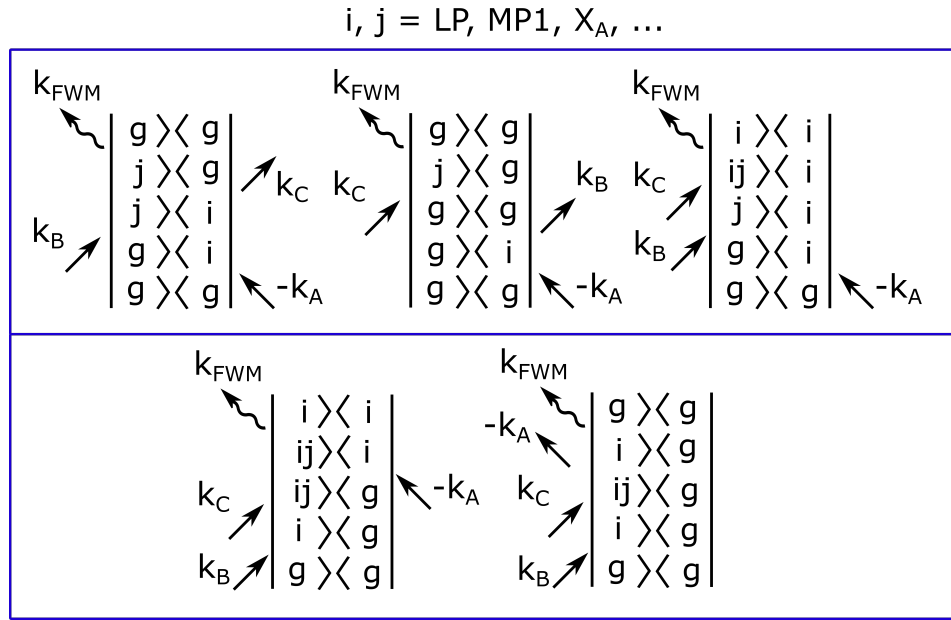


FIG. S8. Double-sided Feynman diagrams showing the excitation pathways contributing to the 1Q rephasing (top) and 2Q non-rephasing spectra (bottom).

* V.Q.C. and E.R.G. are first co-authors

† srimatar@wfu.edu

‡ carlos.silva@umontreal.ca

- [1] F. Thouin, S. Neutzner, D. Cortecchia, V. A. Dragomir, C. Soci, T. Salim, Y. M. Lam, R. Leonelli, A. Petrozza, A. R. S. Kandada, and C. Silva, *Phys. Rev. Mater.* **2**, 034001 (2018).
- [2] F. Thouin, D. Cortecchia, A. Petrozza, A. R. Srimath Kandada, and C. Silva, *Phys. Rev. Res.* **1**, 032032 (2019).
- [3] R. T. Grant, P. Michetti, A. J. Musser, P. Gregoire, T. Virgili, E. Vella, M. Cavazzini, K. Georgiou, F. Galeotti, C. Clark, J. Clark, C. Silva, and D. G. Lidzey, *Adv. Opt. Mater.* **4**, 1615 (2016).
- [4] P. Deshmukh, L. Zhao, S. Satapathy, M. Khatoniar, B. Datta, B. P. Rand, and V. Menon, *Opt. Mater. Express* **13**, 1655 (2023).
- [5] M. Laitz, A. E. K. Kaplan, J. Deschamps, U. Barotov, A. H. Proppe, I. García-Benito, A. Osherov, G. Grancini, D. W. deQuilettes, K. A. Nelson, M. G. Bawendi, and V. Bulović, *Nat. Commun* **14**, 2426 (2023).
- [6] D. B. Straus, S. Hurtado Parra, N. Iotov, J. Gebhardt, A. M. Rappe, J. E. Subotnik, J. M. Kikkawa, and C. R. Kagan, *J. Am. Chem. Soc.* **138**, 13798 (2016).
- [7] H. A. Macleod, *Thin-Film Optical Filters (5th Ed.)* (CRC Press, 2017).
- [8] J. Johansson, P. Nation, and F. Nori, *Comput. Phys. Commun.* **184**, 1234 (2013).
- [9] Y. A. García Jomaso, B. Vargas, D. L. Dominguez, C. L. Ordoñez Romero, H. A. Lara-García, A. Camacho-Guardian, and G. Pirruccio, *Phys. Rev. B* **107**, L081302 (2023).
- [10] T. Kondo, T. Azuma, T. Yuasa, and R. Ito, *Solid State Commun.* **105**, 253 (1998).
- [11] L. Polimeno, A. Fieramosca, G. Lerario, M. Cinquino, M. De Giorgi, D. Ballarini, F. Todisco, L. Dominici, V. Ardizzone, M. Pugliese, *et al.*, *Adv. Opt. Mater.* **8**, 2000176 (2020).
- [12] E. Rojas-Gatjens, K. M. Yallum, Y. Shi, Y. Zheng, T. Bills, C. A. R. Perini, J.-P. Correa-Baena, D. S. Ginger, N. Banerji, and C. Silva-Acuña, *J. Phys. Chem. C* **127**, 15969 (2023).
- [13] L. Mazza, S. Kéna-Cohen, P. Michetti, and G. C. La Rocca, *Phys. Rev. B* **88**, 075321 (2013).
- [14] R. Singh, T. Suzuki, T. M. Autry, G. Moody, M. E. Siemens, and S. T. Cundiff, *Phys. Rev. B* **94**, 081304 (2016).
- [15] X. Li, T. Zhang, C. N. Borca, and S. T. Cundiff, *Phys. Rev. Lett.* **96**, 057406 (2006).
- [16] A. R. Srimath Kandada, H. Li, F. Thouin, E. R. Bittner, and C. Silva, *J. Chem. Phys* **153**, 164706 (2020).
- [17] J. B. Pérez-Sánchez, A. Koner, N. P. Stern, and J. Yuen-Zhou, *Proceedings of the National Academy of Sciences* **120**, e2219223120 (2023).
- [18] K. R. Hansen, C. E. McClure, J. S. Colton, and L. Whittaker-Brooks, *PRX Energy* **1**, 013001 (2022).